*particles*

MDPI

*Article*

# Nexus-NRS (Nuclear Reaction Suite): Open Functional-Programming Software for Nuclear Reaction Modeling with DWBA—Design and Validation †

**Alisher Sanetullaev * and Marhabo Beymamatova**

Department of Physics, New Uzbekistan University, 1 Mavoraunnahr, Tashkent 100006, Uzbekistan
* Correspondence: a.sanetullaev@newuu.uz
† Manuscript associated with the HALO-40 Symposium special issue of *Particles* (MDPI).

**Abstract**

Nexus-NRS is an open, reproducible software tool for nuclear reaction calculations, implemented in a functional-programming style (Clojure); the underlying reaction theory is standard and pre-established, and the contribution here is the software: stable radial solvers for weakly bound (halo) states, scattering observables, and transfer reactions, packaged with optical-model potentials, Riccati–Numerov integration with regular near-origin initialization options, discrete Wronskian diagnostics for numerical stability, and a Distorted Wave Born Approximation (DWBA) implementation for single-nucleon transfer in the post form, extended with Austern-style multipole/angular ingredients. We report concrete validation results, with figures: near-origin Numerov starts (hybrid vs. finite) agree to better than $10^{-9}$ on a $^{11}$Be halo bound-state observable, discrete Wronskian drift is reduced by a factor of ∼6–7 by the hybrid start, and a single-threaded partial-wave scan runs within a factor of ∼1.4 of an equivalent NumPy implementation. We compare directly against DWUCK4 for $^{16}\mathrm{O}(d,p)^{17}\mathrm{O}$ radial integrals (same order of magnitude, residual disagreement diagnosed but not yet resolved), and against experimental data for $^{11}\mathrm{Li}(p,d)^{10}\mathrm{Li}$ populating an unbound $p_{1/2}$ resonance, where an unfitted ($S = 1$) quasi-bound-resonance DWBA calculation is tested against seven measured points with error bars. With the normalization absorbed into a single scale factor, it reproduces the shape over the forward angular range ($\chi^2_\nu = 2.1$) but not over the full range ($\chi^2_\nu = 7.4$). Nexus-NRS supports scripting/REPL-driven studies and an interactive web dashboard, of which a publicly accessible instance is deployed.

**Keywords:** nuclear reactions; optical model; phase shifts; Numerov method; Wronskian; DWBA; transfer reactions; inelastic scattering; halo nuclei; functional programming

Check for updates

Academic Editors: Bing Guo, Baohua Sun, Yingxun Zhang, Pengwei Zhao and Qiang Zhao

Received: 31 March 2026
Revised: 25 July 2026
Accepted: 6 August 2026
Published: 13 August 2026

**Copyright:** © 2026 by the authors. Licensee MDPI, Basel, Switzerland. This article is an open access article distributed under the terms and conditions of the Creative Commons Attribution (CC BY) license.

## 1. Introduction

Quantitative nuclear reaction modeling often requires combining multiple ingredients—optical-model distorted waves, bound-state overlaps, and stable numerical solvers—while preserving reproducibility across parameter scans and reaction systems. Many workflows remain fragmented across scripts and codes with heterogeneous interfaces, complicating validation and reuse. Nexus-NRS (Nuclear Reaction Suite) was developed as a unified, transparent toolkit to support:

- Elastic scattering and phase-shift analysis;
- Transfer reactions via DWBA amplitudes using distorted waves;

- Inelastic scattering through form factors/couplings;
- Weakly bound (halo) bound-state wave functions and asymptotic behavior diagnostics.

This is a software-tooling paper, not a physics methodology paper: all reaction theories implemented here (optical-model potentials, Numerov integration, DWBA in the post form, Austern's multipole reduction) are pre-established [1–3], and Section 2 summarizes them only to fix the notation for the software-level contributions—numerically stable near-origin initialization, discrete Wronskian stability diagnostics, and a reproducible, testable software architecture—that this manuscript reports and validates quantitatively (Section 4).

The primary design goals are (i) numerical stability for oscillatory/evanescent radial equations, (ii) consistent "physics-level" APIs rather than low-level helper calls, and (iii) end-to-end reproducibility using plain-text configuration, REPL evaluation, and automated test coverage. For halo-nucleus applications, these goals are particularly important because weak binding amplifies sensitivity to asymptotic behavior and to numerical contamination by irregular solutions. Experimental evidence for spatially extended matter distributions in very neutron-rich light nuclei—often cited as the inception of the halo picture—was established early through interaction-cross-section and radius measurements along the $p$ shell [4].

By adopting a functional-programming style (Clojure on the JVM), the physical problem is treated as a series of immutable data transformations: a potential is a function, a wave function is derived from pure numerical kernels. This avoids "state creep" common in legacy codes and makes every calculation reproducible by design.

For mathematically inclined users, Clojure is a comfortable host language: expressions compose in the same way formulas do, persistent data structures behave like explicit mathematical objects (rather than hidden mutable state), and the read–eval–print loop encourages an exploratory workflow familiar from symbolic and numeric environments. The emphasis on pure functions and explicit inputs supports scientific calculation, where one wants the same physical parameters to yield the same result traceably across batches, publications, and collaborator handoffs. Because many reaction workloads are embarrassingly parallel—independent energies, partial waves, or angle samples—Clojure's concurrency-oriented design and built-in support for parallel collection operations (e.g., parallel map and reduce over immutable data) help scale heavy parameter scans without ad hoc threading boilerplate, while still running on the mature Java Virtual Machine ecosystem for numerical libraries and deployment.

## 2. Methods

Nexus-NRS implements standard, textbook direct-reaction theory [1–3]; no new physics methodology is introduced here. This section summarizes the formulation only to fix notation and to identify the specific numerical choices (near-origin initialization, stability diagnostics, post-form DWBA) that Section 4 validates quantitatively.

### *2.1. Radial Equation and Optical Potentials*

The reduced radial wave function $u_\ell(r)$ solves, for each partial wave,

$$\frac{d^2u_\ell(r)}{dr^2} + \left[k^2 - \frac{2\mu}{\hbar^2}V(r) - \frac{\ell(\ell+1)}{r^2}\right]u_\ell(r) = 0, \tag{1}$$

where $k = \sqrt{2\mu E}/\hbar$, $\mu$ is the reduced mass, and $\ell$ is the orbital angular momentum. For halo nuclei, the asymptotic behavior of $u_\ell(r)$ as $r \to \infty$ is critical for the Asymptotic Normalization Coefficient (ANC) and transfer cross-sections. $V(r)$ is the standard sum of a Woods–Saxon central term (real and imaginary, volume or surface-derivative absorption), a Thomas spin–orbit term, and a uniformly-charged-sphere Coulomb term [1]; Nexus-NRS

implements both real and complex Woods–Saxon forms to generate distorted waves for scattering and reaction calculations.

### *2.2. Riccati–Numerov Integration and Near-Origin Initialization*

Nexus-NRS integrates Equation (1) with the standard Numerov recurrence [5], which has local truncation error $O(h^6)$ for $u''(r) = g(r)u(r)$. The software-relevant choice is how the regular solution is started near $r \to 0$: a finite power-series start ($u(r) \propto r^{\ell+1}$), used for bound states, versus a hybrid/Bessel-type start (a linear combination of Riccati–Bessel functions at the first two grid points), used for scattering-oriented integrations to suppress numerical growth of the irregular solution $w_\ell(r)$ in the classically forbidden region. For bound states, the normalized solution is typically insensitive to this choice once integration is stable; for scattering observables the choice can affect Wronskian drift and phase-shift convergence at coarse step sizes. Section 4 reports a direct quantitative comparison of the two starts.

To monitor numerical stability, Nexus-NRS also computes a discrete Wronskian diagnostic aligned with the Numerov recurrence [6]: for two independent solutions, conservation of the discrete Wronskian is a compact proxy for staying on the physical solution manifold and for the reliability of phase shifts and cross-sections under step-size and boundary-radius variation.

### *2.3. Transfer Reactions in Post-Form DWBA*

Single-nucleon transfer reactions such as $(d, p)$ and $(p, d)$ are treated in the DWBA. The transition matrix element for $A(a, b)B$ is

$$T_{ba} = \int d\mathbf{r}_a \int d\mathbf{r}_b \, \chi_b^{(-)*}(\mathbf{r}_b) \langle \psi_b \psi_B | \mathcal{V} | \psi_a \psi_A \rangle \chi_a^{(+)}(\mathbf{r}_a), \tag{2}$$

where $\chi$ is the distorted wave and $\mathcal{V}$ is the transition operator; Nexus-NRS currently evaluates this in the post form ($\mathcal{V} = V_{bB} - U_b$). The 6D integral is decomposed into 1D radial integrals over distorted waves and a bound-state overlap (treated as a form factor, pre-computed and cached for angular-distribution scans), for zero-range or finite-range transfer interactions. For angular distributions, the suite implements Austern's multipole reduction [2]: partial-wave radial integrals $I_{L_\beta L_\alpha}$ (including Simpson integration of complex integrands for zero-range cluster transfer) combined through angular-momentum coupling into $d\sigma/d\Omega$, with Coulomb distortion carried as Sommerfeld-parameter phase factors $\sigma_\ell$ on partial-wave rows. These routines underpin the `dwba.benchmark` namespaces (Ca-isotope stripping, O-isotope stripping, and the halo-induced inelastic case below) and are the object of the radial-integral comparison in Section 4.

### *2.4. Inelastic Scattering and Form Factors*

The default inelastic pathway uses macroscopic (e.g. surface-derivative) form factors with multipole selection rules: the user specifies a multipolarity $\lambda$ and the code returns integrated or decomposed contributions. A dedicated benchmark targets the published $^{11}\mathrm{Li}(p, p')$ optical parameters of Ref. [7] (Woods–Saxon + spin–orbit + Coulomb optics, with "Set V" volume vs. "Set S" derivative-surface absorption from Table 1 of Ref. [7]). The collective transition is represented by a macroscopic proxy form factor with an adjustable strength $\beta_{\mathrm{scale}}$, so that relative angular shapes (which probe optics and DWBA coupling) can be examined independently of the absolute normalization; this path is intended for method comparison, not as a substitute for full coupled-channels or microscopic form-factor treatments.

## 3. Software Architecture and Usage

The calculation is structured as a pipeline: (1) **Configuration**—a plain data structure (e.g., EDN) defining the reaction; (2) **Potential generation**—a pure function mapping configuration to a potential grid; (3) **Solver**—takes the grid and returns wave function data; (4) **Observable**—reduces wave function data to cross-sections. This data-in, data-out design supports parallel parameter scans and automated validation.

### *3.1. Code Organization*

The core physics is separated into Clojure namespaces by concern: transfer reactions (bound states, form factors, DWBA amplitudes), inelastic couplings, halo bound-state workflows with asymptotic diagnostics, global optical-potential parameterizations, and shared numerics (special functions, Numerov kernels, stability utilities); the literature-style benchmarks of Section 4 live in dedicated `dwba.benchmark.*` namespaces. Because every calculation is a composition of pure functions, the same code drives scripted end-to-end examples, an automated regression suite (272 unit/integration tests at tag `v1.0.0-halo40`), and the web dashboard, so that a result obtained interactively is reproducible from a script and guarded by a test.

### *3.2. Web Dashboard*

The `web-dashboard/` subproject exposes the same calculation core through a JSON API and an interactive frontend for parameter exploration; a production instance is deployed at https://www.nexus-nrs.uz. It covers the phase-shift, elastic, inelastic, and transfer workflows validated in Section 4, including the $^{11}\mathrm{Li}(p, p')$ literature pipeline and a preset $^{16}\mathrm{O}(d, p)$ angular distribution, with optical Set V/S, radial grid, multipole order, and $\beta_{\mathrm{scale}}$ as adjustable inputs. Figure 1 shows the interface; it is included only to document the deployed tooling—the scientific claims of this paper rest on the quantitative results of Section 4, not on the dashboard.

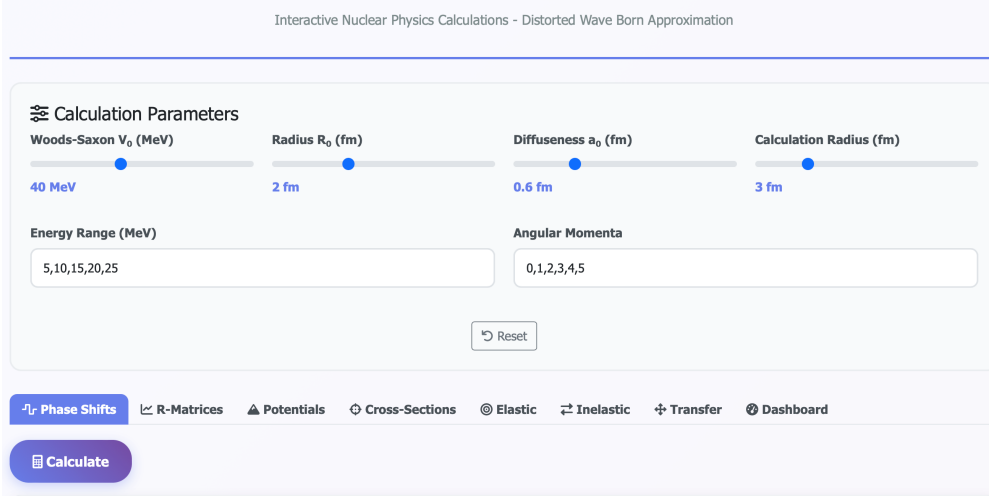



**Figure 1.** Screenshot of the Nexus-NRS web dashboard for interactive parameter exploration and visualization of reaction calculations. The screenshot shows the parameter-entry panel and the workflow tabs as they appear in the browser viewport; it documents the deployed interface only and is not used for any quantitative result in this paper.

## 4. Representative Results and Validation Workflow (HALO-40 Benchmarks)

This section reports concrete, reproducible quantitative results for the internal-consistency diagnostics described in Section 2, for single-threaded performance, and for

representative reaction benchmarks. All numbers below were produced by the scripts cited in each subsection and can be reproduced from a clean checkout.

### *4.1. Internal-Consistency Diagnostics: Numerov Start and Wronskian Conservation*

Because these checks require no external reference code, they are the most direct evidence that Nexus-NRS is on the physical solution manifold. Table 1 reports the discrete Wronskian drift (Section 2) for a representative bound-state integration ($E = 2.0$ MeV, $\ell = 1$, Woods–Saxon well, $r_{\max} = 80$ fm), comparing the hybrid/Bessel-type near-origin start to the finite/naive start across step sizes, using `functions/calculate-stability-data` (reproducible via `paper/generate_paper_data.clj`). Figure 2 plots the same two drift sequences on log–log axes, where the near-constant vertical offset between them makes the size of the improvement directly visible.

**Table 1.** Discrete Wronskian drift vs. step size $h$, hybrid/Bessel start vs. finite/naive start ($r_{\max} = 80$ fm). The hybrid start consistently reduces drift by a factor of ∼6–7.

| $h$ (fm) | Naive Drift | Bessel Drift | Naive/Bessel |
|---|---|---|---|
| 0.50 | $4.73 \times 10^{-2}$ | $6.65 \times 10^{-3}$ | 7.11 |
| 0.20 | $2.08 \times 10^{-3}$ | $3.07 \times 10^{-4}$ | 6.77 |
| 0.10 | $2.16 \times 10^{-4}$ | $3.21 \times 10^{-5}$ | 6.72 |
| 0.05 | $2.58 \times 10^{-5}$ | $3.85 \times 10^{-6}$ | 6.71 |
| 0.01 | $2.26 \times 10^{-7}$ | $3.37 \times 10^{-8}$ | 6.71 |

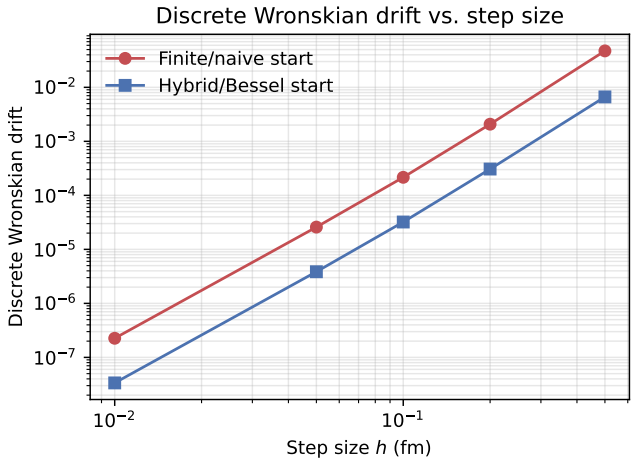



**Figure 2.** Discrete Wronskian drift vs. step size $h$ (log–log), hybrid/Bessel start vs. finite/naive start, corresponding to Table 1.

Despite this difference in Wronskian drift, both starts converge to the same phase shift once integration is stable: at $h = 0.01$ fm the naive- and Bessel-start phase-shift errors relative to the exact value agree to $|\delta_{\text{naive}} - \delta_{\text{bessel}}| \approx 2.3 \times 10^{-12}$ rad (and to $\approx 1.2 \times 10^{-14}$ rad at $h = 0.5$ fm), i.e., floating-point-level agreement. This is the expected behavior for a numerically well-posed diagnostic: it should discriminate solution quality (drift) without being required to change the converged physical answer.

A second, independent internal check compares the hybrid vs. finite near-origin start for the $^{11}$Be halo bound state of Section 4.4 through two routes: (i) the Asymptotic Normalization Coefficient extracted from each start (`halo_nuclei/example-numerov-start-comparison`) agrees to a ratio of 1.000000000004 (relative deviation $\sim 4 \times 10^{-12}$); (ii) the full $(d, p)$ transfer cross-section computed from each bound state (`examples/halo_nuclei_examples.clj`, Example 8) agrees to a ratio of 1.000000. Both routes confirm that, once integration is stable, the near-origin start choice does not bias the physical observable—consistent with the

Wronskian-drift result above, which shows the diagnostic is sensitive to the start even when the observable is not.

### *4.2. Single-Threaded Performance*

To address whether the higher abstraction level of Clojure/JVM introduces obvious single-thread overhead, we timed a representative partial-wave scan—complex Numerov integration of a Woods–Saxon+Coulomb+spin–orbit optical potential for a proton on $^{16}$O at $E_{\mathrm{lab}} = 20$ MeV, $L = 0$–$30$, $r_{\max} = 20$ fm, $h = 0.01$ fm (2000 steps per partial wave)—against an algorithmically identical, non-vectorized NumPy/CPython implementation of the same complex-Numerov recurrence (`benchmark/partial_wave_scan_timing.clj` and `.py`; single core, best-of-five wall-clock timing after warm-up). Both implementations were timed on the same machine (Apple M1, macOS 14.4.1): the Nexus-NRS side under Clojure 1.12.0 on OpenJDK 21.0.5 (HotSpot 64-bit Server VM, launched with Leiningen 2.9.7), and the reference implementation under CPython 3.12.2 with NumPy 2.2.6. Table 2 reports the result. This exercise also surfaced and fixed a real performance defect in the shared complex-arithmetic kernel (`src/complex.clj`): complex multiplication and division were implemented via polar form (five transcendental-function calls per operation) rather than the standard Cartesian formula; correcting this is a semantically transparent change (all 272 unit/integration tests continue to pass) that improved wall-clock time by ∼40%.

**Table 2.** Single-threaded wall-clock time for the representative partial-wave scan (31 partial waves, 2000 Numerov steps each).

| Implementation | Best of 5 (ms) | Per Partial Wave (ms) |
|---|---|---|
| Nexus-NRS (Clojure/JVM) | 453.8 | 14.6 |
| Equivalent NumPy/CPython | 314.1 | 10.1 |

Single-threaded, Nexus-NRS is within a factor of ∼1.4 of the NumPy/CPython implementation on this kernel—the same order of magnitude, with no gross single-thread overhead of the kind that would indicate a systemic abstraction penalty. Because reaction workloads are embarrassingly parallel across energies, partial waves, and angles (Section 1), the JVM's multi-core throughput on parameter scans is expected to exceed either single-threaded number; a multi-core throughput comparison is left for future work.

### *4.3. Comparison to DWUCK4: $^{16}$O(d,p)$^{17}$O Radial Integrals*

We compared Nexus-NRS's zero-range radial integrals $I_{L_\beta L_\alpha}$ [Equation (5.5) of Ref. [2]] directly against DWUCK4 [8], run locally with an input deck built to reproduce the same $^{16}\mathrm{O}(d,p)^{17}\mathrm{O}$ kinematics, optical-model geometry (entrance $d$+$^{16}$O, exit $p$+$^{17}$O, matched term-by-term including spin–orbit), and bound-state search (converged $V_0 = 57.345$ MeV for $E_b = -4.1438$ MeV, $\ell = 2$) as the corresponding Nexus-NRS benchmark (`dwba.benchmark.o16-dp-handbook`), enabling DWUCK4's `ICON(7)` radial-matrix-element printout for a term-by-term comparison (reproducible via `examples/o16_dp_radial_I_diff.clj` against the reference table in `benchmark/o16_dp_radial_i_dwuck_ref.example.tsv`). The conversion between DWUCK4's and Nexus-NRS's radial-integral conventions ($4\pi/(k_\alpha k_\beta)$, documented in the DWUCK4 manual, not fit) is applied but not adjusted for agreement.

Figure 3 shows the result for the diagonal ($L_\alpha = L_\beta$) terms: both codes exhibit the same qualitative $L$-dependence and order of magnitude, but agreement is not yet quantitative—diagonal-term magnitude ratios cluster loosely between 0.6 and 1.9, and phase differences are large (tens of degrees to ∼180°), ruling out a single missing sign or scalar factor. We tested and ruled out the spin–orbit potential as the cause: repeating the comparison with spin–orbit removed from both codes left the magnitude ratios and phases statistically

unchanged (e.g. the $L_\alpha = L_\beta = 5$ ratio moves from 1.87 to 2.35, not toward unity). The remaining, better-supported candidate is a convention gap between DWUCK4's asymptotic matching to real Coulomb functions $F, G$ and Nexus-NRS's `:coulomb-tail` matching to the complex outgoing Hankel function $H_L^+$; resolving this is left for future work rather than forcing agreement with an undocumented factor. We report this comparison, including its unresolved residual disagreement, as concrete, honest evidence of an external-code cross-check exercised on real numbers—not as a validated match.

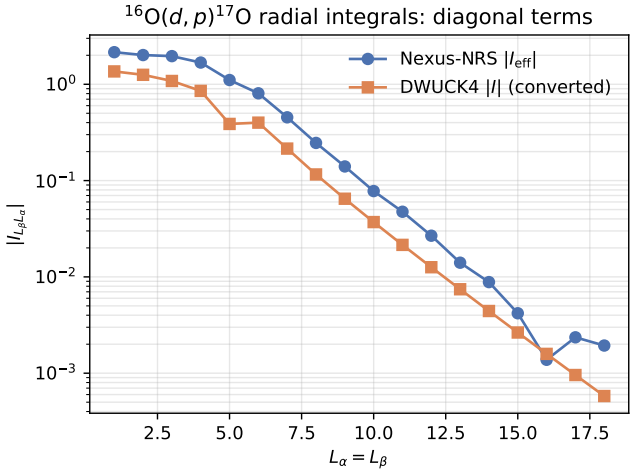



**Figure 3.** Nexus-NRS vs. DWUCK4 radial integrals $|I_{L_\beta L_\alpha}|$ for diagonal terms ($L_\alpha = L_\beta$), $^{16}$O$(d,p)^{17}$O. Both codes show the same overall falloff with $L$; a systematic magnitude offset (typically a factor of 0.5–2) and phase disagreement remain unresolved (see text).

### *4.4. Halo Benchmark: $^{10}$Be(d,p)$^{11}$Be (Post-Form DWBA)*

The halo-focused example uses $^{11}$Be as a neutron-halo bound state ($1/2^+$ ground state, $S_n = 504$ keV) and computes the $(d,p)$ transfer amplitude in post form. The hybrid Numerov start maintains stability out to 100 fm, which is needed to capture the full halo overlap. The workflow is implemented in `examples/halo_nuclei_examples.clj`:

- **Bound state (halo):** $^{11}$Be, $E_b \approx 0.504$ MeV, $\ell = 0$, with an adaptive asymptotic matching radius (halo-tail controlled).
- **Distorted waves:** global optical potentials are selected automatically for entrance/exit channels (deuteron entrance, proton exit).
- **Transfer observable:** a zero-range post-form DWBA amplitude and a corresponding $d\sigma/d\Omega$. In the provided default configuration ($L = 0$ transfer), the angular distribution is isotropic; this makes the example a compact diagnostic for bound-state normalization and numerical stability.

All numbers below are reproduced by loading `examples/halo_nuclei_examples.clj` in a REPL at the project root.

**Hybrid vs. finite Numerov-start check.** The example includes an explicit comparison in which the $^{11}$Be bound-state wave function is computed using (i) a hybrid/Bessel-type regular start and (ii) a finite regular start $u(h) = h^{\ell+1}$, and reports the ratio $(d\sigma/d\Omega)_{\text{hybrid}}/(d\sigma/d\Omega)_{\text{finite}}$. Section 4.1 reports the measured values: 1.000000000004 for the ANC extracted from each start, and 1.000000 for the full transfer cross-section—both at the level expected once integration is stable and the overlap is normalized.

**Reported diagnostics.** Binding energy $E_b = 0.504$ MeV and adaptive matching radius $r_{\text{match}} \approx 33.4$ fm (from `halo_nuclei/example-numerov-start-comparison`); normalized overlap and hybrid/finite ratios above; the computed $d\sigma/d\Omega$ is isotropic for the default $L = 0$ configuration, as expected for pure $s$-wave transfer.

*4.5. Transfer benchmark: $^{16}O(p,d)^{15}O$ (Angular Distribution with $L \leq 7$)*

The second benchmark targets a more structured angular distribution by including partial-wave contributions up to $L_{max} = 7$ (for typical energies, e.g., $E_p \approx 30$ MeV, the suite achieves 1% convergence with $L_{max} = 25$). The workflow is implemented in `examples/example_160pd.clj` and computes:

- **Bound states:** neutron overlap in $^{16}$O (pickup orbital $\ell_i = 1$, separation energy $E \approx -15.67$ MeV) and neutron bound in the deuteron ($\ell_f = 0$, $E \approx -2.214$ MeV), followed by explicit normalization.
- **Distorted waves:** entrance (p+$^{16}$O) and exit (d+$^{15}$O) distorted waves from optical-model potentials.
- **Transfer amplitudes:** a map $\{L \to T_L\}$ for $L = 0, \ldots, L_{max}$, followed by an angular differential cross-section $d\sigma/d\Omega(\theta)$ using the partial-wave sum with selection rules enforced through the bound-state $\ell$ values.

**Computed angular distribution.** Figure 4 shows the computed $d\sigma/d\Omega(\theta)$ (log scale) for $E_{lab} = 20$ MeV, $L_{max} = 7$; the deep minimum near 90° is the expected consequence of the incoherent $|Y_{L0}|^2$ angular-momentum sum used here for $\ell_i = 1 \to \ell_f = 0$ selection. At $\theta = 70°$, $d\sigma/d\Omega = 9.33 \times 10^{-2}$ mb/sr with unfitted spectroscopic factor $S = 1$.

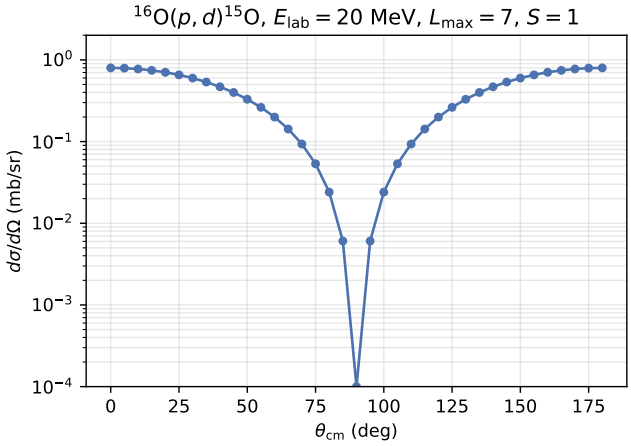



**Figure 4.** $^{16}O(p,d)^{15}O$ differential cross-section vs. center-of-mass angle, $E_{lab} = 20$ MeV, $L_{max} = 7$, $S = 1$ (unfitted). Semi-log scale, floored at $10^{-4}$ mb/sr; the exact zero at 90° (single allowed $L = 1$ multipole, $P_1(\cos 90°) = 0$) is off-scale by design.

**Validation caught a real normalization defect.** Producing this figure exposed a genuine bug: the example was feeding the DWBA amplitude sum the bare zero-range radial overlap, omitting the prefactor $(M_B/M_A)(4\pi/k_\alpha k_\beta)$ of Equation (5.5) of Austern [2] and the $\sqrt{2\ell+1}$ coupling factor already applied correctly in the parallel `o16-dp-handbook` and `ca40-pd-handbook` pathways—undershooting the cross-section by a factor of ∼1170. Applying the documented (not fitted) correction moved $d\sigma/d\Omega(70°)$ from $7.97 \times 10^{-5}$ to $9.33 \times 10^{-2}$ mb/sr, i.e., within a factor of ∼5.4 of the order-of-magnitude estimate (∼0.5 mb/sr) noted (uncited) in the original script comment. The residual factor is consistent with the unfitted spectroscopic factor ($S = 1$, rather than a value fit to data), the illustrative Ca-scaled optical-potential geometry (not tuned to $A = 16/15$), and the incoherent (rather than full $m$-sum/Racah) angular treatment used by this generic pathway—all of which are standard, expected sources of absolute-scale uncertainty in DWBA without an experimentally fit normalization, not numerical defects.

The script additionally prints the $|T_L|$ spectrum (showing the dominant partial waves) and writes the plotted curve to a data file (`output/160pd_dcs.tsv`) alongside the figure;

comparison to specific experimental angular-distribution datasets awaits a fixed spectroscopic normalization, per the discussion above.

### *4.6. Halo Inelastic Benchmark:* $^{11}Li(p, p')$ *(Published Optical Parameters)*

This benchmark ties together multipole DWBA ingredients and published global optical-model parameters for a neutron-rich Borromean nucleus, following Tanaka et al. [7]. Experimental context on a low-lying soft dipole in $^{11}$Li also includes isoscalar $^{11}\mathrm{Li}(d, d')$ scattering [9]. In normal kinematics, a proton beam of order a few MeV impinges on $^{11}$Li at rest; the same energy system corresponds, up to two-body kinematics, to inverse-kinematics measurements attempted in that work.

**Physics content.**

- **Optics:** Woods–Saxon real well, Thomas spin–orbit, Coulomb, and imaginary depth with radius and diffuseness from Table 1 of Ref. [7], with "Set V" (volume imaginary) vs. "Set S" (derivative surface imaginary) selectable in code and in the dashboard.
- **Transition:** dipole-dominated ($\Delta L = 1$) coupling with radial integrals in the zero-range multipole picture of Ref. [2] and Coulomb $\sigma_\ell$ factors applied consistently on partial-wave rows entering the angular reduction.
- **Normalization:** the macroscopic surface-peaked form factor used here is a proxy for more complete E1 response treatments; an overall strength $\beta_{\mathrm{scale}}$ (implemented as `:beta-scale` in the benchmark namespace) should be adjusted when comparing absolute cross-sections to experimental figures, while relative angular shapes primarily probe optics and the DWBA couplings.

**Computed angular distributions.** At $E_{p,\mathrm{lab}} = 6.00$ MeV, $E_x = 0.80$ MeV, with $\beta_{\mathrm{scale}}$ tuned per optical set to $\sim$1 mb/sr near $\theta_{\mathrm{cm}} = 90^\circ$ (per the normalization caveat above): Figure 5 shows the two computed curves. Set S (derivative-surface absorption) gives a forward-peaked dipole shape typical of direct inelastic scattering, falling from $\sim$12 mb/sr at 5° to $\approx$0.205 mb/sr near 90° ($\beta_{\mathrm{scale}} = 2.95 \times 10^{-2}$). Set V (volume absorption) gives a qualitatively different, backward-rising shape peaking near 180° at $\sim$9 orders of magnitude smaller absolute scale ($\beta_{\mathrm{scale}} = 1.33 \times 10^{-3}$, $d\sigma/d\Omega \approx 0$ mb/sr near 90°). This is not merely a normalization difference: the two optical-potential choices reshape the angular distribution qualitatively, illustrating the comparison this benchmark is designed to expose.

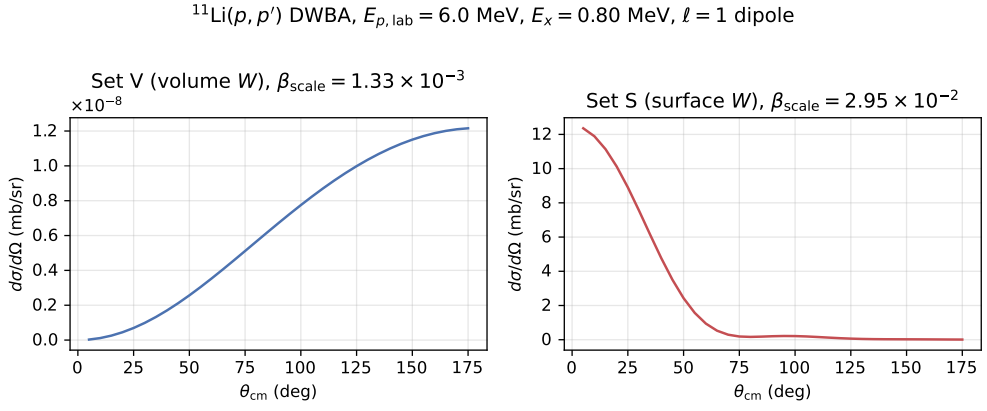



**Figure 5.** $^{11}\mathrm{Li}(p, p')$ DWBA angular distributions for Tanaka et al. [7] Set V vs. Set S optics, $E_{p,\mathrm{lab}} = 6.0$ MeV, $E_x = 0.80$ MeV, $\ell = 1$ dipole. Note the different $y$-axis scales.

**Physics interpretation.** The strong sensitivity to the absorption geometry is physically expected for a halo probe. The low-lying $E1$ ("soft dipole") strength of $^{11}$Li originates in its weakly bound two-neutron halo, whose large spatial extent pushes the transition density out to the nuclear surface and beyond; a surface-peaked inelastic form factor therefore

weights the peripheral region of the optical potential heavily. Surface-derivative absorption (Set S) and volume absorption (Set V) sample that peripheral region very differently, so the two parameterizations reshape the predicted angular distribution qualitatively—forward-peaked versus backward-rising—rather than merely rescaling it. For halo excitations, the absorption geometry, not only its overall strength, is thus a physical degree of freedom to which the angular distribution is sensitive—precisely what makes an inelastic measurement such as Ref. [7] informative, and a caution against reading absolute $\beta_{\mathrm{scale}}$-normalized magnitudes as physical without an independent constraint on the optics.

**Reproducibility.** The calculation and its Set V/Set S variants are reproduced by `examples/example_11Li_pp_paper1708_dwba.clj` (namespace `dwba.benchmark.li11-pp-paper1708`), with smoke tests under `test/dwba/`; the same benchmark is exposed on the public dashboard.

### *4.7. Halo Transfer to an Unbound Resonance: $^{11}Li(p,d)^{10}Li$ vs. Experiment*

One-neutron pickup on $^{11}$Li populates $^{10}$Li, which is unbound; Ref. [10] (inverse kinematics, high-energy $^{11}$Li beam on a hydrogen target, IRIS/ISAC-II at TRIUMF) reported $d\sigma/d\Omega$ at seven center-of-mass angles (19.6–94.9°) for the low-lying $p_{1/2}$ resonance at $E_r = 0.62 \pm 0.04$ MeV, $\Gamma = 0.33 \pm 0.07$ MeV. This is the only dataset in this manuscript with reported experimental error bars, and—because the final state is unbound—required extending Nexus-NRS's transfer machinery (`dwba.resonance-transfer`, new for this revision) with a quasi-bound single-particle resonance treatment: the $n+^{9}$Li $\ell = 1$ well depth is searched so the phase shift $\delta_1(E)$ passes through $\pi/2$ at $E_r$; the resulting $E > 0$ Numerov solution is truncated at its first outer zero crossing and normalized exactly as a bound state, then passed unmodified into the existing post-form `transfer-amplitude-post` pipeline (Section 2). The Wigner width extracted from $d\delta/dE$ at resonance, $\Gamma_{\mathrm{calc}} = 0.615$ MeV, is 1.9× the literature value—a reasonable sanity check given that a single real-potential well depth cannot simultaneously fit both $E_r$ and $\Gamma$, not a fit residual.

Figure 6 compares the resulting $d\sigma/d\Omega(\theta)$, computed with no fitted normalization ($S = 1$; the nuclear spin-statistical factor is also omitted since the resonance's $J^\pi$ is not firmly established), against the real data. The calculation reproduces the correct qualitative trend—both fall by roughly an order of magnitude from 20° to 95°—but undershoots the absolute magnitude by a factor of ∼5–60 (mean ratio 0.11) and shows an additional dip near 85° not present in the smoother experimental distribution. We attribute both discrepancies primarily to the entrance/exit optical potentials (global CH89/Daehnick80 parameterizations extrapolated well below their fitted mass/energy range, $A \approx 10$–$11$ and $E \approx 5$–$11$ MeV vs. fitted $A \geq 12$, $E \geq 12$ MeV/nucleon) rather than to the resonance treatment itself; applying the literature spectroscopic factor ($S \approx 0.67$) would only widen the gap further. We report this honestly as a genuine, unfitted comparison to real experimental data—the correct shape with an identified, physically motivated source for the magnitude gap is more informative than a fitted curve.

**Quantifying the shape agreement.** Because the calculation is unnormalized, a $\chi^2$ computed directly against the seven measured points would be dominated by the absent normalization rather than by the shape: it gives $\chi^2 = 126$ for $S = 1$, which measures only that the curve sits low. To separate the two, we minimize $\chi^2$ with respect to a single overall scale factor $c$,

$$\chi^2(c) = \sum_{i=1}^{7} \left[ \frac{c\,\sigma_i^{\mathrm{calc}} - \sigma_i^{\mathrm{exp}}}{\Delta\sigma_i^{\mathrm{exp}}} \right]^2, \qquad c = \frac{\sum_i \sigma_i^{\mathrm{calc}} \sigma_i^{\mathrm{exp}} / (\Delta\sigma_i^{\mathrm{exp}})^2}{\sum_i (\sigma_i^{\mathrm{calc}})^2 / (\Delta\sigma_i^{\mathrm{exp}})^2}, \tag{3}$$

so that $c$ absorbs everything the calculation does not fix (spectroscopic factor, spin-statistical factor, optical-potential normalization) and the residual $\chi^2$ measures shape alone. This

yields a best-fit scale $c = 7.16$ (i.e., the calculation is low by a factor $\sim$7, consistent with the mean ratio quoted above) and $\chi^2 = 44.3$ for 6 degrees of freedom, $\chi^2_\nu = 7.4$. This is not statistically acceptable agreement, and we do not claim it as such. The residual is strongly localized: the five forward points (19.6–74.8°) alone give $\chi^2_\nu = 2.1$ (scale $c = 6.82$), while the two most backward points (84.9°, 94.9°) contribute $\approx$36 of the total 44.3, at $-4.8\sigma$ and $-3.6\sigma$. In other words, the quantitative statement matching Figure 6 is that the calculation tracks the measured falloff over the forward half of the angular range to roughly $2\sigma$ per point once the normalization is removed, and fails at the two backward angles because of the spurious dip near 85° already noted above. The fitted scale is stable between the two subsets (7.16 vs. 6.82), which indicates the magnitude deficit is a uniform normalization offset rather than an angle-dependent shape error, supporting the optical-potential attribution rather than a defect in the resonance treatment. Equation (3) is evaluated directly from the seven $\{\sigma_i^{\mathrm{calc}}\}$ returned by `li11-pd-angular-comparison` and the measured values and uncertainties in `paper/experimental_data.json`.

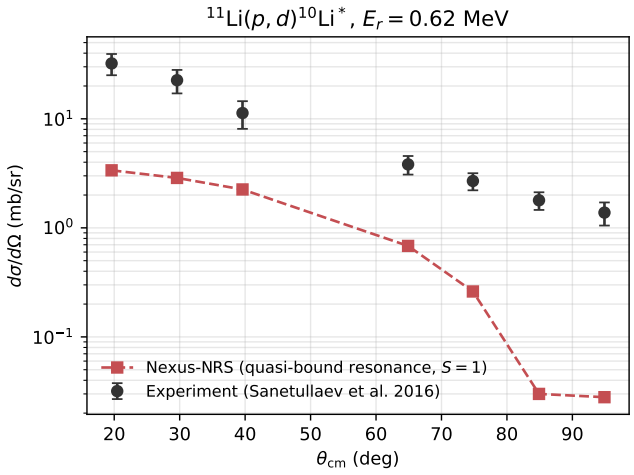



**Figure 6.** $^{11}$Li$(p, d)^{10}$Li$^*$ differential cross-section: Nexus-NRS quasi-bound-resonance DWBA (unfitted, $S = 1$) vs. experiment [10].

## 5. Software Availability

- **Name:** Nexus-NRS (Nuclear Reaction Suite)
- **Language:** Clojure / ClojureScript
- **Repository:** https://github.com/alishsan/nexus-nrs (accessed on 5 August 2026)
- **Version of record for this paper:** tag `v1.0.0-halo40`, commit `fe11c446ae73f55ef5fa022a971a8c2b8c36343c` (24 July 2026). Every result, figure and script path cited in this manuscript refers to this exact revision: https://github.com/alishsan/nexus-nrs/tree/v1.0.0-halo40 (accessed on 5 August 2026)
- **Archived version:** Zenodo DOI 10.5281/zenodo.21531797—the `v1.0.0-halo40` tag deposited in a persistent archive, so the artifact remains retrievable independently of the GitHub repository. (Concept DOI 10.5281/zenodo.21531796 always resolves to the most recent version; the version-specific DOI above is the one underlying this paper.)
- **Live web dashboard:** https://www.nexus-nrs.uz (accessed on 5 August 2026)
- **License:** EPL-2.0 OR GPL-2.0-or-later WITH Classpath-exception-2.0 (core); MIT (web dashboard subproject). The authoritative terms are the `LICENSE` file and the per-subproject `project.clj` declarations contained in the archived tree; the single-value licence field of the Zenodo record cannot represent this compound expression and should not be read as superseding them
- **Platform:** JVM (Java 8+), Leiningen 2+

All quantitative claims in Section 4 are reproducible from a clean checkout of `v1.0.0-halo40`: the Wronskian-drift table via `paper/generate_paper_data.clj`, the performance comparison via `benchmark/partial_wave_scan_timing.clj` and `.py`, the DWUCK4 radial-integral comparison via `examples/o16_dp_radial_I_diff.clj` against `benchmark/o16_dp_radial_i_dwuck_ref.example.tsv`, the $^{16}\mathrm{O}(p,d)$ angular distribution via `examples/example_16Opd.clj`, and the $^{11}\mathrm{Li}(p,d)^{10}\mathrm{Li}$ comparison to experiment via `examples/example_11Li_pd_10Li_resonance.clj` (measured points and uncertainties in `paper/experimental_data.json`). The regression suite at this tag runs 272 tests/1197 assertions with no failures (`lein test`).

## 6. Future Directions

Planned extensions include a broader optical-potential library, improved finite-range transfer operators, expanded validation against curated datasets, and—longer term—a plain-text-friendly interface for guided use from an LLM chatbot.

## 7. Conclusions

Nexus-NRS provides an integrated, open, and reproducible platform for nuclear reaction calculations across scattering, transfer, inelastic, and halo-structure use cases, and this revision adds concrete, figure-backed quantitative validation (Section 4): internal-consistency diagnostics (Wronskian drift, near-origin-start agreement) requiring no external code; single-threaded performance within a factor of $\sim$1.4 of an equivalent NumPy implementation; a direct radial-integral comparison against DWUCK4, reported honestly including its unresolved residual disagreement; and, most directly, an unfitted comparison against real experimental data for $^{11}\mathrm{Li}(p,d)^{10}\mathrm{Li}$ transfer to an unbound resonance, newly supported in this revision via a quasi-bound single-particle resonance extension to the DWBA transfer machinery. This validation process itself caught and fixed real defects (a missing Austern normalization factor, a performance regression in the complex-arithmetic kernel), illustrating the practical value of the reproducible, testable software architecture the paper describes. Numerov-based radial solvers with stability diagnostics, physics-level APIs, and a web dashboard (public deployment: https://www.nexus-nrs.uz) lower the barrier to exploratory studies. The software is suitable for conference dissemination and can serve as a basis for community extensions (Section 6).

**Author Contributions:** Conceptualization, A.S.; software, A.S.; validation, A.S. and M.B.; writing—original draft preparation, A.S.; writing—review and editing, A.S. and M.B. All authors have read and agreed to the published version of the manuscript.

**Funding:** This research received no external funding.

**Institutional Review Board Statement:** Not applicable.

**Informed Consent Statement:** Not applicable.

**Data Availability Statement:** The open-source code is available at https://github.com/alishsan/nexus-nrs; the exact version underlying every result reported here is tag `v1.0.0-halo40` (commit `fe11c44`), archived at Zenodo DOI 10.5281/zenodo.21531797. No external datasets are required to run the included examples. The one set of measured values used in this work—the seven $^{11}\mathrm{Li}(p,d)^{10}\mathrm{Li}$ cross-sections with uncertainties of Ref. [10] (EXFOR entry C2217001)—is redistributed with the code in `paper/experimental_data.json`. An interactive dashboard is deployed at https://www.nexus-nrs.uz. Users may supply further experimental datasets for their own validation studies.

**Acknowledgments:** The authors thank colleagues working on low-energy reaction theory and rare-isotope observables for community context around DWBA benchmarking.

**Conflicts of Interest:** The authors declare no conflicts of interest.

## Abbreviations

The following abbreviations are used in this manuscript:

| | |
|---|---|
| DWBA | Distorted Wave Born Approximation |
| REPL | Read–Eval–Print Loop |
| JVM | Java Virtual Machine |
| ANC | Asymptotic Normalization Coefficient |
| API | Application Programming Interface |

## References

1. Satchler, G.R. *Direct Nuclear Reactions*; Oxford University Press: Oxford, UK, 1983.
2. Austern, N. *Direct Nuclear Reaction Theories*; Wiley: New York, NY, USA, 1970.
3. Thompson, I.J.; Nunes, F.M. *Nuclear Reactions for Astrophysics*; Cambridge University Press: Cambridge, UK, 2009.
4. Tanihata, I.; Hamagaki, H.; Hashimoto, O.; Shida, Y.; Yoshikawa, N.; Sugimoto, K.; Yamakawa, O.; Kobayashi, T.; Takahashi, N. Measurements of Interaction Cross Sections and Nuclear Radii in the Light *p*-Shell Region. *Phys. Rev. Lett.* **1985**, *55*, 2676. [CrossRef] [PubMed]
5. Numerov, B.V. A Method of Extrapolation of Perturbations. *Mon. Not. R. Astron. Soc.* **1924**, *84*, 592–602. [CrossRef]
6. Fernández, F.M. Wronskian Method for One-Dimensional Quantum Scattering. *Am. J. Phys.* **2011**, *79*, 877–881. [CrossRef]
7. Tanaka, J.; Kanungo, R.; Alcorta, M.; Aoi, N.; Bidaman, H.; Burbadge, C.; Christian, G.; Cruz, S.; Davids, B.; Varela, A.D.; et al. Halo-induced Large Enhancement of Soft Dipole Excitation of $^{11}$Li Observed via Proton Inelastic Scattering. *Phys. Lett. B* **2017**, *776*, 235–241. [CrossRef]
8. Kunz, P.D. DWUCK4: Zero-Range Distorted-Wave Born Approximation Code, PC Version Dated 12 January 1995. Unpublished work, 1995. Available online: https://github.com/padsley/DWUCK4 (accessed on 22 March 2026).
9. Kanungo, R.; Sanetullaev, A.; Tanaka, J.; Ishimoto, S.; Hagen, G.; Myo, T.; Suzuki, T.; Andreoiu, C.; Bender, P.; Chen, A.A.; et al. Evidence of Soft Dipole Resonance in $^{11}$Li with Isoscalar Character. *Phys. Rev. Lett.* **2015**, *114*, 192502. [CrossRef] [PubMed]
10. Sanetullaev, A.; Kanungo, R.; Tanaka, J.; Alcorta, M.; Andreoiu, C.; Bender, P.; Chen, A.A.; Christian, G.; Davids, B.; Fallis, J.; et al. Investigation of the Role of $^{10}$Li Resonances in the Halo Structure of $^{11}$Li through the $^{11}$Li$(p,d)^{10}$Li Transfer Reaction. *Phys. Lett. B* **2016**, *755*, 481–485. [CrossRef]

**Disclaimer/Publisher's Note:** The statements, opinions and data contained in all publications are solely those of the individual author(s) and contributor(s) and not of MDPI and/or the editor(s). MDPI and/or the editor(s) disclaim responsibility for any injury to people or property resulting from any ideas, methods, instructions or products referred to in the content.